applied sciences

MDPI

Article

Properties of Barium Silicate Obtained by Microwave–Hydrothermal (M-H) Method

Volodya V. Baghramyan [1,*], Cristina Leonelli [2,*], Cecilia Mortalò [3], Tatiana S. Azatyan [1], Agapi A. Petrosyan [1], Alkhas A. Ghazaryan [1], Tatevik V. Grigoryan [1] and Anahit A. Sargsyan [1]

[1] Institute of General and Inorganic Chemistry After M.G. Manvelyan, NAS of Armenia, Yerevan 0051, Armenia; asargis@mail.ru (A.A.S.)
[2] Department of Engineering "Enzo Ferrari", University of Modena and Reggio Emilia, Via Pietro Vivarelli 10, 41125 Modena, Italy
[3] Institute of Condensed Matter Chemistry and Technologies for Energy (ICMATE), National Research Council of Italy (CNR), Corso Stati Uniti 4, 35127 Padova, Italy; cecilia.mortalo@cnr.it
* Correspondence: v_bagramyan@mail.ru (V.V.B.); cristina.leonelli@unimore.it (C.L.)

Abstract

A microwave–hydrothermal (M-H) method was developed for synthesizing barium silicate from solutions of barium salts and sodium silicate. Advanced techniques (DTA, XRD, IR spectroscopy, SEM and TEM) were used to study the optical, granulometric, electrical and other functional characteristics of barium silicate. $BaSiO_3$ synthesized at 100 °C is an amorphous nano-sized powder (10–20 nm); however, the product synthesized at 240 °C has a crystalline structure (20–27 nm), whereas the crystalline phase of $BaSiO_3$ is typically obtained using known methods at temperatures above 400 °C (12–40 nm). During M-H synthesis, it was found that the structure formation mechanism and particle size of $BaSiO_3$ changed due to the peculiar features of microwave heating. The synthesized barium metasilicate exhibits a high diffuse reflectance coefficient of 92%. It is a wide-band-gap semiconductor with a band gap width of Eg = 4.1 eV. Both amorphous and crystalline phases of $BaSiO_3$ exhibit high photocatalytic activity in the UV range. This study shows that the developed M-H method enables the production of nano-sized powder and enhances the functional properties of barium silicate. Compared with conventional methods, the M-H method is more efficient due to reduced synthesis time and lower energy costs.

Keywords: microwave-hydrothermal (M-H) synthesis; barium silicate; nanoparticles; photocatalysis; diffuse reflectance

Academic Editor: Antony C. Calokerinos

Received: 30 December 2025
Revised: 11 February 2026
Accepted: 14 February 2026
Published: 18 February 2026

1. Introduction

In a $BaO–SiO_2$ system, various barium silicates (Ba_2SiO_4, $BaSiO_3$, $BaSi_2O_5$, Ba_3SiO_5, $Ba_5Si_8O_4$) are formed, which exhibit high chemical and thermal stability but differ in structural diversity [1–5]. Barium silicates are widely used in the production of phosphors for light-emitting diodes, fluorescent lamps, photovoltaic cells, plasma screens, etc. [6–10]. These materials are also utilized in the technology for producing barium glasses and barium cements [6,7,11–14]. The high-temperature glasses and ceramics obtained from them are used in various fields of modern technology, such as nuclear energy, rocket engineering, jet aviation, instrumentation, and more [13,14].

It should be noted that the methods for obtaining barium silicates are technologically complex and require significant energy expenditure [9,10,15–19]. Barium silicates are primarily produced through solid-phase high-temperature synthesis (1100 °C and above),

involving the interaction of barium carbonate ($BaCO_3$) or barium oxide (BaO) with silicon dioxide (SiO_2) [1,3,5,9,15–18]. They can also be obtained using hydrothermal *sol–gel* methods based on the formation of a solid phase in a liquid medium by interaction of barium salts with silica-containing reagents (such as silica gel, tetraethoxysilane, or sodium silicate $Na_2SiO_3 \cdot 9H_2O$), followed by prolonged calcination of the resulting substances [19–24].

Barium hydrosilicates are obtained through a hydrothermal method by interacting reagents in a SiO_2–NaOH–$BaCl_2$–H_2O system [20,21]; however, the latter undergoes some hydrolysis in hot water. To increase the yield of barium silicate, synthesis from $BaCl_2$ and Na_2SiO_3 was conducted at 20 °C in an alcohol–water medium [20–24]. Thermal treatment was then performed to obtain the crystalline phase: at 800 °C, nano-sized crystals of barium silicates (Ba_2SiO_4 and $BaSiO_3$) had already formed. This enabled the authors [20] to obtain crystalline barium metasilicate with a yield of up to 95%.

Disadvantages of solid-phase synthesis include high temperatures (1200–1400 °C) during processing, which result in low product homogeneity and contamination. The sol–gel method yields homogeneous nanomaterials, but it relies on expensive starting precursors (barium and silicon alkoxides). The technology is complex, requiring control of pH, hydrolysis rate, and temperature. It is also time-consuming and results in a very low yield. Hydrothermal synthesis is energy-efficient, but it requires high pressures (typically 10–100 MPa). Reproducing the morphology is difficult because the particle size and shape depend heavily on the conditions. Other phases may also form with even slight changes in temperature, pressure, or solution composition. The SHS (self-propagating high-temperature synthesis) method [25–27] is also well known for silicate synthesis. It is fast and energy-saving, but difficult to control and produces inhomogeneous products.

One of the key challenges in modern chemistry and materials science is the development of new synthesis methods that reduce energy consumption and shorten process times [28,29]. In this context, microwave (MW)-assisted chemistry is a promising approach that opens up new opportunities in synthesis technology [30–42]. Advantages of MW-assisted chemistry include high speed, uniform heating of the entire reaction medium volume, absence of contact between the heated body and the heating source, high energy-to-heat conversion efficiency, no gaseous emissions or environmental pollution, reduced energy consumption, and shorter target material production times.

In the case of silicates specifically, based on the literature and our previous work [30–32,42–44] describing microwave–hydrothermal preparation of sub-micrometric zeolite crystals and nano-sized zinc and zirconium silicates, and reporting that microwave heating produces relatively narrow crystal size distributions and requires much shorter heating times without significantly altering composition, crystallinity or surface chemistry compared to conventional hydrothermal methods, we expected to observe several advantages in this work. This work aimed to utilize the capabilities of microwave chemistry for the liquid-phase synthesis of barium silicates. We therefore anticipated reducing energy costs and improving their functional properties [31–43]. Analysis of the scientific and technical literature, as well as our own research, shows that microwave synthesis can reveal new properties of known compounds, thereby expanding their scope of application.

This work aims to develop a microwave–hydrothermal (MH) method for synthesizing barium silicate by interactions between aqueous solutions of barium chloride and sodium silicate. To the best of our knowledge, there are no published reports on the hydrothermal–microwave synthesis of barium silicate. Therefore, we carefully characterized the powders obtained in this study using several techniques, including differential thermal analysis (DTA), spectroscopic methods, photocolorimetry, flame photometry, transmission electron microscopy (TEM), scanning electron microscopy (SEM) and X-ray diffraction for phase analysis.

2. Materials and Methods

Barium metasilicate, $BaSiO_3$, was synthesized in Samsung CE1073AR and MS-6 microwave ovens (NPO VOLTA, St. Petersburg, Russia) operating at a frequency of 2.45 GHz with an output power of 600 W. This was achieved by interactions of aqueous solutions of sodium silicate and barium chloride in a stoichiometric ratio via the precipitation method. Low-temperature reactions (up to the boiling point of the aqueous solutions) were conducted in a microwave oven (Samsung Electronics & Co. Ltd, Suwon, Republic of Korea) using an open Pyrex® glass flask equipped with a reflux condenser and a stirrer. The flask was loaded with an initial solution of 300 mL of 0.5 M sodium silicate and the reaction temperature was raised to 95–100 °C. Barium chloride solution (0.5 M) was added until the pH reached 8–8.5, with a reaction time of 30 min. Microwave synthesis at higher temperatures (up to 240 °C) was conducted in a Teflon™ vessel in a commercial lab-dedicated MS-6 microwave oven (Milestone, Bergamo, Italy). The pressure and temperature were controlled via an automatic Peltier cell provided by the oven manufacturer and immersed in the reaction medium. The obtained solid phase (target product) was filtered and washed with cold distilled water ($\leq$14 °C) to remove Na^+ and Cl^- ions. It was then dried at 150 °C.

The thermal treatment of the samples obtained at 100 °C and atmospheric pressure was carried out in an LHT 08/17 electric furnace (Nabertherm GmbH, Lilienthal, Germany).

The composition and characteristics of the final products were determined using physicochemical analysis methods. X-ray diffraction (XRD) analysis of the samples was performed using the powder method on a high-resolution X-ray diffractometer (SmartLab, Rigaku Holding Co. Ltd., Akishima-shi, Tokyo, Japan) setup with CuKα radiation. Differential thermal and thermogravimetric analyses were conducted using a simultaneous TGA/DSC apparatus (TGA/DSC 3+, Mettler Toledo, Columbus, OH, USA).

IR spectra of the samples in the range of 400–4000 cm^{-1} were obtained using a Fourier-transform IR spectrometer Cary 630 (USA). Scanning electron microscopy (SEM) analyses were conducted using a high vacuum microscope (Philips XL 40, Thermo Fisher Scientific, Waltham, MA, USA). Transmission electron microscopy (TEM) studies were carried out using a high-resolution scanning/transmission electron microscope (S/TEM) (Talos™ F200S, Thermo Fisher Scientific, Waltham, MA, USA), which was equipped with energy dispersive X-ray spectroscopy (EDS) and operated at an acceleration voltage of 200 kV. Powders were dispersed in distilled water (Milli-Q® IQ 7000, MilliporeSigma, Burlington, MA, USA) and suspensions were obtained by sonicating for 15 min. The specimens were prepared by immersing 200 mesh nickel microscope grids and dried by IR lamp before the analyses.

Diffuse reflection of the samples was determined using a Cary 60 UV–Vis Spectrophotometer (Agilent Technologies, Santa Clara, CA, USA). The specific surface area and pore volume of the samples were measured by nitrogen adsorption using the BET method on an "AccuSorb 2300E" analyzer (Micromeritics Instruments Corp, Norcross, GA, USA) and by the gravimetric method of benzene vapor adsorption. The UV radiation source for photocatalysis was a Navigator lamp with a power of 25 W and a maximum emission at λ = 253.7 nm. The reactor for studying photocatalysis was a quartz glass vessel with a volume of 300 mL and a diameter of 80 mm. The optical density of the dye solutions was measured using a Cary 630 FT-IR spectrometer (Agilent Technologies, Santa Clara, CA, USA).

3. Results

3.1. Mineralogical Composition

X-ray diffraction showed that the material obtained at 100 °C is amorphous (see Figure 1a). On the other hand, the pattern of the sample obtained at 240 °C displayed sharper, more intense reflections that match those of $BaSiO_3$ (ICDD 26-1402), as observable in Figure 1b. The

broad background and relatively weak peaks suggest a nanocrystalline structure containing a significant amorphous phase. No additional peaks were observed, which confirms the absence of any secondary phases and the product's single-phase composition.

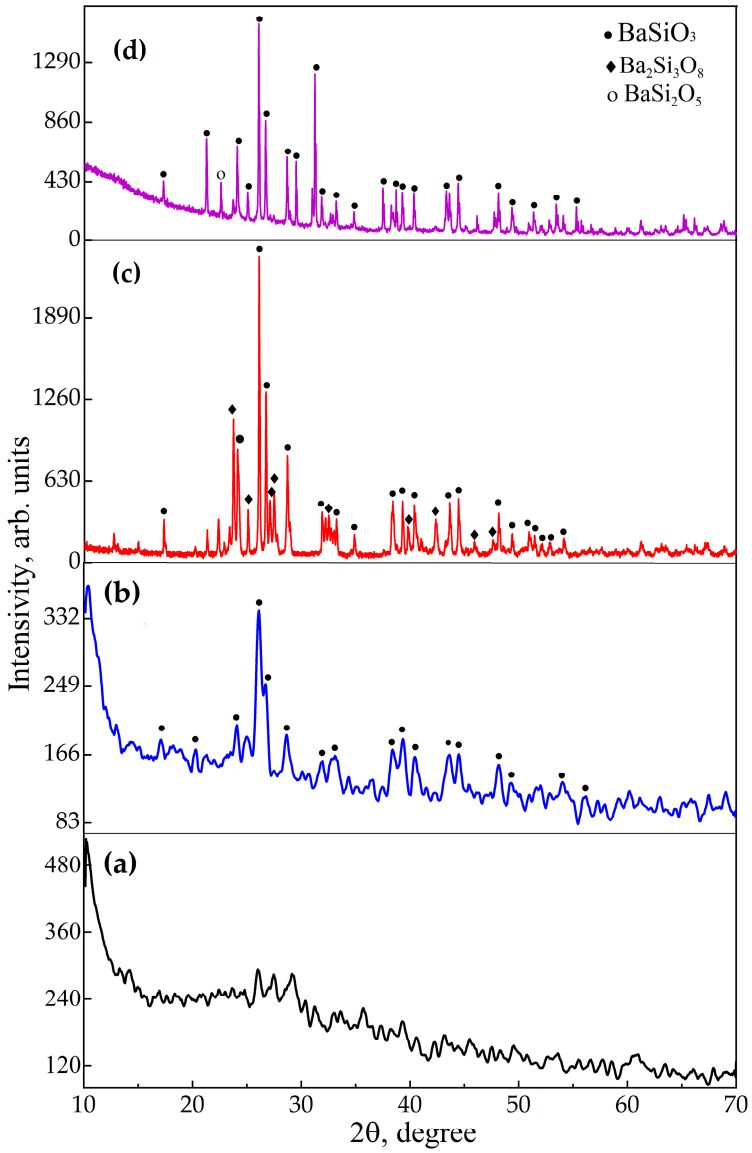

Figure 1. X-ray diffraction pattern of barium metasilicate: (**a**) Sample obtained at 100 °C with MW and dried at 150 °C; (**b**) Sample obtained at 240 °C with MW and dried at 150 °C; (**c**) Sample obtained at 100 °C with MW and calcined at 800 °C; (**d**) Sample obtained at 100 °C with MW and calcined at 1000 °C.

After annealing at 800 °C, the product exhibited narrower peaks and consisted mainly of $BaSiO_3$, with SiO_2 and Ba_2SiO_4 present in smaller amounts (Figure 1c). Following annealing at 1000 °C for 2 h, the material was predominantly crystalline $BaSiO_3$ with minor amounts of $BaSi_2O_5$ and Ba_2SiO_4 (Figure 1d). This phase evolution is consistent with compositions approaching the limits of the BaO–SiO_2 system.

Slight deviations from perfect stoichiometry may occur during drying (e.g., the formation of $BaCO_3$ and SiO_2). Upon heating, $BaCO_3$ decomposes, which can result in the

redistribution of components and the formation of phases with different Ba:Si ratios (e.g., $BaSi_2O_5$, Ba_2SiO_4), according to the following reaction:

$$BaSiO_3\ (s) + SiO_2\ (s) \rightarrow BaSi_2O_5\ (s)$$

$$BaSiO_3\ (s) + BaO(s) \rightarrow Ba_2SiO_4\ (s)$$

This is consistent with the transformations observed by XRD upon calcination.

The distinctive feature of microwave synthesis is the formation of the crystalline phase of barium metasilicate at the relatively low temperature of 240 °C (30–33 atm) (see Figure 1b). Using conventional methods, the crystalline phase of barium silicate is typically only achieved at temperatures above 400 °C [1–6,24].

3.2. Thermogravimetric Analysis

Figure 2 compares the thermograms of samples synthesized at 100 °C and 240 °C, both of which were dried at 150 °C. The sample obtained at 100 °C showed a gradual mass loss of 1.3% up to 200 °C (including 0.8% up to 150 °C), which is attributable to adsorbed water taken up during cooling (Figure 2b). In contrast, the crystalline sample synthesized at 240 °C showed no mass change up to 200 °C, indicating the absence of adsorbed moisture (Figure 2a).

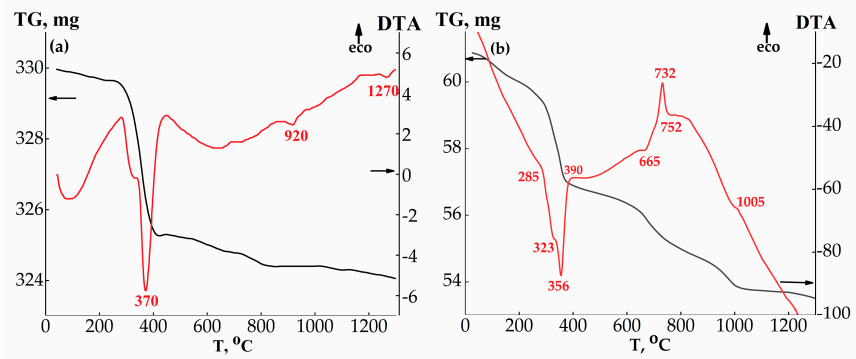

Figure 2. TG (weight loss in g) and DTA (mV) curves of barium metasilicate: (**a**) MW synthesis at 240 °C, dried at 150 °C; (**b**) MW synthesis at 100 °C, dried at 150 °C. (Black lines are for TG and red lines are for DTA).

At higher temperatures, the weight losses observed for both materials were due to the removal of bound/crystalline water from barium hydrosilicates. This stepwise dehydration is consistent with the formation of hydrates reported for the BaO–SiO_2–H_2O system (e.g., $BaO{\cdot}SiO_2{\cdot}6H_2O$, $BaO{\cdot}SiO_2{\cdot}3H_2O$, $BaO{\cdot}SiO_2{\cdot}1.5H_2O$, $BaO{\cdot}SiO_2{\cdot}H_2O$).

The endothermic signals at 325, 356, 370 and 665 °C arise from structural rearrangements associated with the progressive dehydration of these hydrates. The exothermic peak at 732 °C (visible for the sample prepared at 100 °C, see Figure 2b) corresponds to the crystallization of $BaSiO_3$, as confirmed by X-ray diffraction. This event is absent in the sample synthesized at 240 °C, as it was already crystalline (see Figure 2a).

An endothermic effect near 920 °C is consistent with crystallite growth/ordering or a possible polymorphic transformation of $BaSiO_3$. A weak exotherm around 1005 °C, together with the accompanying mass loss, is attributed to the decomposition of $BaCO_3$ and subsequent oxygen removal, leading to defect-rich $BaSiO_3$.

A further weak exotherm near 1270 °C reflects the high-temperature microstructural evolution of barium silicate and may indicate incongruent melting [2].

3.3. FT-IR Analysis

The FT-IR spectra of air-dried and thermally treated $BaSiO_3$ are shown in Figure 3. They were interpreted in light of the literature [21,22,45,46]. For the crystalline sample, a complex set of bands appears between 600 and 1000 cm^{-1}, including features at ~960 cm^{-1} and ~882 cm^{-1} corresponding to (Si–O–Si) and (O–Si–O), respectively (see Figure 3). An intense band near 500 cm^{-1} (compared with ~448 cm^{-1} in the amorphous sample) is attributable to deformation modes of the Si–O, Si–O–Ba and Ba–O bonds. Weak bands were also observed in the 600–700 cm^{-1} region (symmetric Si–O–Si bridges), and maxima at ~731 and ~690 cm^{-1} are consistent with a metasilicate-chain anion. In amorphous material, the Si–O vibration is centred near 1010 cm^{-1}, whereas in the crystalline sample, it splits and shifts to 961 and 882 cm^{-1}, consistent with SiO_4 tetrahedra (see Figure 3).

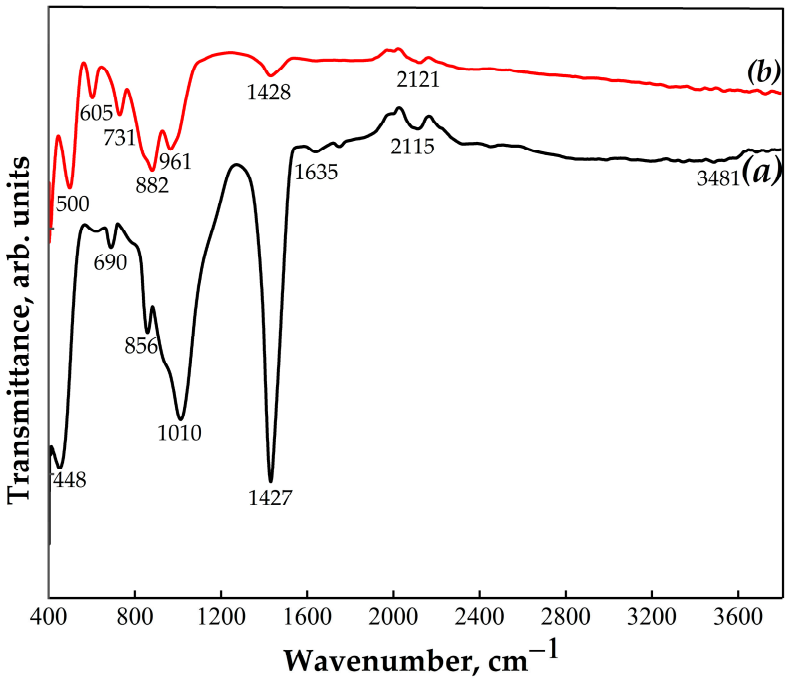

Figure 3. IR spectra of barium silicate: **a**—Sample obtained at 100 °C with MW and dried at 150 °C; **b**—Sample obtained at 100 °C with MW and calcined at 1000 °C.

The 1010 cm^{-1} maximum is lower than the 1100 cm^{-1} position typical of pure SiO_2, indicating Si–O–Ba bonding. Bands at ~856 and ~882 cm^{-1} are assigned to Ba–O–Si deformations. The O–H stretching vibration (3000–3500 cm^{-1}) and H_2O bending vibration (~1635 cm^{-1}) are absent after calcination at 1000 °C, consistent with dehydration. Signatures of carbonate at ~1428 and ~690 cm^{-1} are evident in dried powders, but these become weaker after thermal treatment, which is consistent with the formation of $BaCO_3$ upon drying and its subsequent decomposition upon heating.

3.4. Morphological and Microstructural Observations

Electron microscopy confirms that microwave synthesis produces nano-sized $BaSiO_3$. TEM analysis of a sample produced at 100 °C reveals particles measuring ~10–20 nm (see Figure 4a). Scanning electron microscopy (SEM) of the material synthesized at 100 °C and subsequently heat-treated at 1000 °C reveals a densified, sintered microstructure with characteristic particle sizes of around 50 nm (Figure 4b).

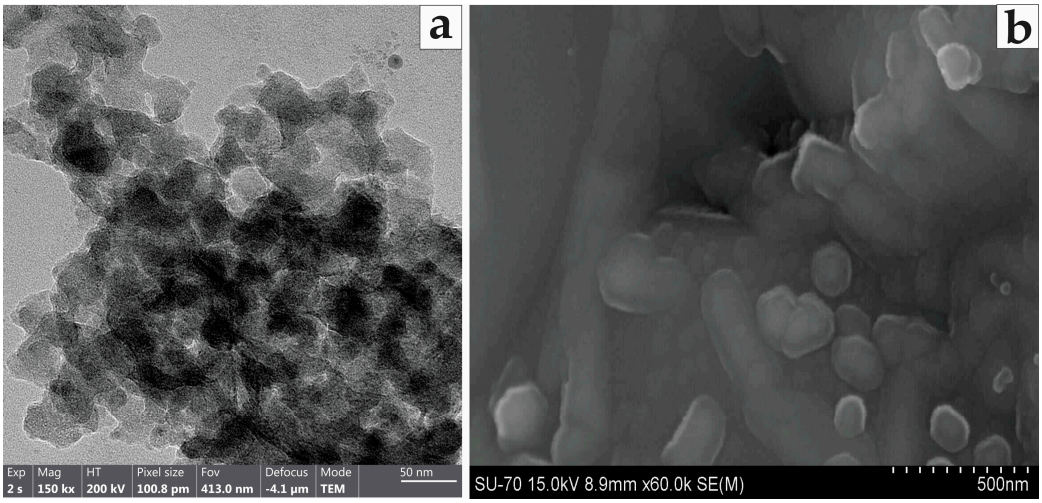

Figure 4. TEM (**a**) image and SEM (**b**) image of barium silicate.

Crystallite sizes estimated from XRD using the Scherrer equation are consistent with nanoscale dimensions: ~20–30 nm for the sample synthesized at 100 °C and dried; ~30–32 nm after heat treatment at 800 °C; and ~20–27 nm for the crystalline sample obtained directly at 240 °C. Calcination led to particle coarsening, accompanied by a reduction in specific surface area and pore volume (from ~202 to ~15.2 m^2/g and from ~0.016 to ~0.0055 cm^3 respectively), consistent with densification.

3.5. Photocatalytic Characterization

Diffuse-reflectance spectra (200–900 nm) show high reflectance (~90%) in the visible/near-IR for all $BaSiO_3$ powders (Figure 5). The reflection coefficients of the synthesized barium silicate samples in the visible and near-infrared regions of the spectrum are approximately 90%. The amorphous sample exhibits slightly higher reflectance than the crystalline material obtained at 1000 °C, attributable to particle agglomeration during crystallization. Absorption bands (Figure 6) were observed in the UV region of the spectrum, possibly due to the presence of additional barium silicate phases, as suggested by XRD (Figure 1).

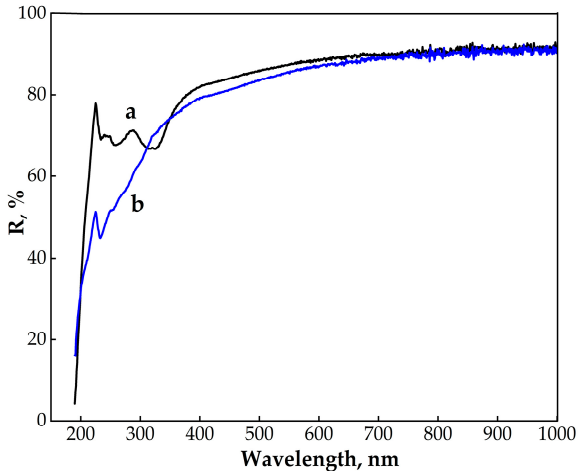

Figure 5. Diffuse reflectance spectra of powdered $BaSiO_3$: **a**—dried at 150 °C and **b**—heat-treated at 1000 °C.

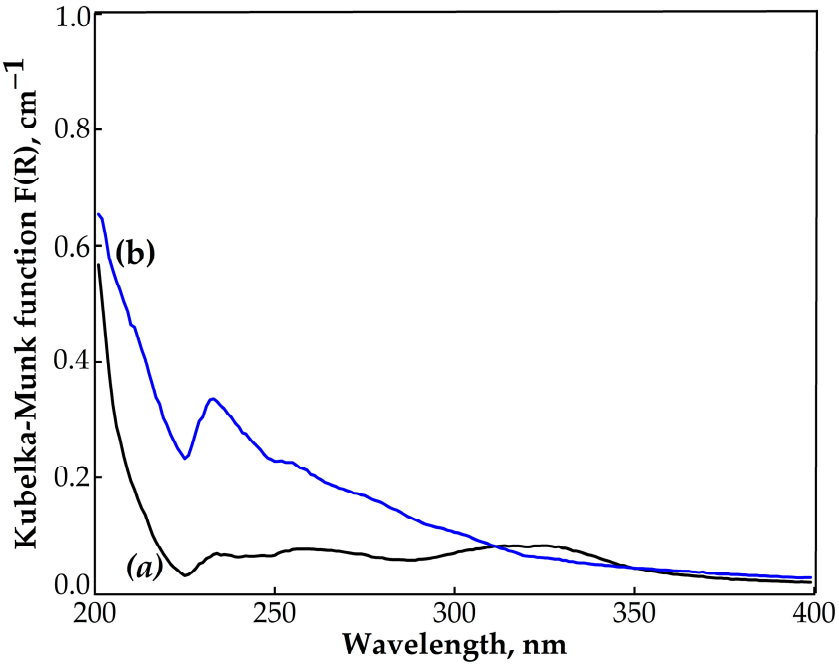

Figure 6. Absorption spectra of powdered $BaSiO_3$ samples recalculated using the Kubelka–Munk function F(R): **a**—sample obtained at 100 °C and dried at 150 °C and **b**—sample obtained at 100 °C and calcined at 1000 °C.

From the diffuse reflectance spectra, the absorption spectra were obtained by recalculating the Kubelka–Munk function F(R) (Figure 7) using the formula:

$$F(R) = (1 - R)^2/2R \quad (1)$$

where (R) is proportional to the absorption coefficient.

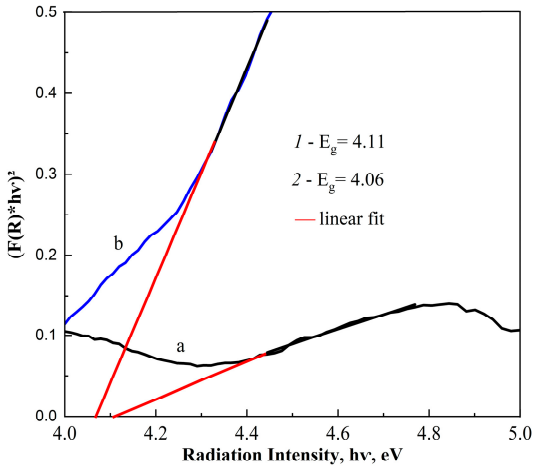

Figure 7. Dependence curves (F(R) * hv)^2 vs. photon energy hv for powdered $BaSiO_3$ samples: **a**—sample obtained at 100 °C and dried at 150 °C and **b**—sample obtained at 100 °C and calcined at 1000 °C.

Thus, the diffuse reflectance coefficient R is converted into an equivalent absorption coefficient using the modified Kubelka–Munk function F(R). At the same time, the band

gap of the material can be determined by extrapolating the linear portion of the $(\alpha h\upsilon)^{1/n}$ dependence on hν with the energy axis $h\upsilon$ of the incident light:

$$F(R) * h\upsilon = A\ (h\upsilon - Eg)^n \quad (2)$$

where A is a proportionality constant related to the nature of the material, h is Planck's constant, and $n = 1/2$ for direct allowed transitions. Figure 7 presents the curves of the dependence of $(F(R) * h\upsilon)^2$ on the light energy hν, obtained using diffuse reflectance spectra and calculations based on Formulas (1) and (2). The band gap energy Eg for the studied samples was determined by extrapolating the linear segments of these curves to their intersection with the $h\upsilon$ axis.

The presented data indicate that the samples have a similar band gap width, at 4.11 eV and 4.06 eV for samples dried at 150 °C and heat-treated at 1000 °C, respectively. Therefore, the average band gap value of the synthesized material (barium metasilicate) is Eg = 4.09 eV. According to the literature, barium metasilicate is a wide-band-gap dielectric with a band gap width of 3.46–4.3 eV [19].

It is well known that nanoscale materials exhibit new functional properties. In particular, dielectric nanostructures demonstrate high photocatalytic activity across a wide spectrum and the ability to accumulate photo-generated charge carriers. In dielectrics, absorption of a photon leads to valence electrons transitioning to the conduction band, forming an electron-hole pair that can participate in the oxidation of organic compounds adsorbed on the dielectric surface. Catalytic activity depends on the number of photo-induced electrons that reach the dielectric surface. The degree of recombination of holes and electrons in the conduction band of nanoparticles is significantly reduced, thereby increasing their catalytic activity. The photocatalytic activity of the synthesized barium metasilicate was studied in the methylene blue (MB) degradation reaction under UV irradiation. The degree of decomposition of the MB was determined by measuring the optical density of the centrifuged solution (MB solution after centrifugation) before and after UV irradiation in the presence of the synthesized catalyst ($BaSiO_3$). Experimentally, it was established that the dependence of the solution's optical density on the MB concentration is linear. Figure 8 shows the optical densities of methylene blue solutions at various wavelengths before and after UV irradiation at different times (from 5 to 90 min), using amorphous and crystalline samples of $BaSiO_3$ as catalysts.

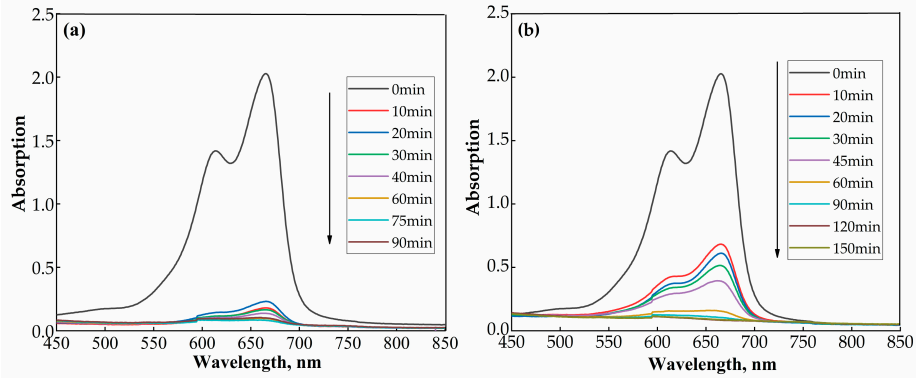

Figure 8. Dependence of optical density on wavelength at different UV irradiation times, in the presence of the catalyst ($BaSiO_3$): (**a**) amorphous, (**b**) crystalline.

Based on this, the kinetics of the photocatalytic destruction of MB was determined from the optical density values of the solution at a wavelength of 664 nm, which corresponds to the maximum light absorption by the MB dye. Preliminary experiments were carried out to determine the photocatalytic properties of the synthesized barium silicate under

the following conditions: 10 mg of $BaSiO_3$, a concentration of 10 mg/L of MB, a solution volume of 100 mL, a wavelength of 253.4 nm and a power of 25 W of UV radiation. Figure 9 shows the curves of the degree of MB photodecomposition as a function of time. It can be seen that the photocatalytic activities of amorphous and crystalline barium metasilicate are almost the same. The degree of decomposition of methylene blue through 45 min with the amorphous catalyst and after 60 min with the crystalline catalyst is 90–92%.

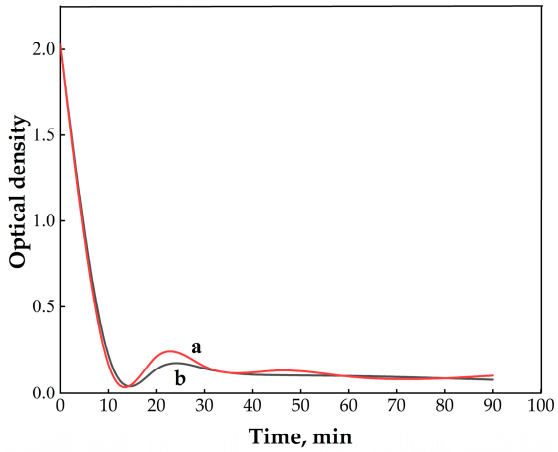

Figure 9. Dependence of the degree of decomposition of MB on the exposure time to UV radiation in the presence of the $BaSiO_3$ catalyst: **a**—amorphous (dried at 150 °C), **b**—crystalline (treated at 1000 °C).

4. Discussion

Microwave–hydrothermal synthesis was used to prepare nano-sized barium metasilicate from water-soluble precursors at a low temperature. The product is amorphous at 100 °C (the boiling point), whereas a crystalline $BaSiO_3$ phase forms at 240 °C. In both cases, the powders are nanodispersed (≈10–27 nm) (see Figure 1a,b).

A mechanistic perspective on rapid crystallization and particle size control is presented. In a microwave field, rapid volumetric heating uniformly raises the temperature of the entire reaction medium, quickly achieving the required supersaturation for nucleation. This promotes a burst of near-simultaneous nucleation throughout the volume and limited subsequent growth, yielding smaller, more uniform particles with reduced aggregation compared to stepwise, wall-mediated heating. The rapid volumetric heating also increases the partial pressure of water vapour within the micropores of the forming solid. This generates autogenous pressure, which facilitates early crystallization at comparatively low external temperatures and pressures. Accordingly, a crystalline $BaSiO_3$ phase is observed at 240 °C (~30–32 atm) under MW-hydrothermal conditions. While the fast temperature increase under MW irradiation produces a rapid and uniform nucleation and growth rate with a peculiarly narrow particle size dispersion and morphology, as discussed in the literature [47,48], isolating the particles unambiguously is challenging. Here, however, the dominant effects can be explained by the fast and uniform heating and pressure build-up that are inherent to MW processing.

At higher temperatures, stepwise mass losses correspond to the dehydration of barium hydrosilicates. Endothermic events at ~325, 356, 370 and 665 °C reflect structural rearrangements during progressive dehydration. An exotherm at ~732 °C (for the 100 °C sample) marks the crystallization of $BaSiO_3$, which is consistent with XRD. This event is not present in the 240 °C sample, which is already crystalline. An endotherm near 920 °C is consistent with crystallite growth/ordering or a possible polymorphic transformation. A weak exotherm near 1005 °C, together with mass loss, is attributed to the decomposition of $BaCO_3$ and subsequent oxygen removal, leading to defect-rich $BaSiO_3$. A further

weak exotherm near 1270 °C reflects high-temperature microstructural evolution, which is potentially related to incongruent melting.

The FT-IR analysis support the formation of $BaSiO_3$: indeed, the spectra shown in Figure 3 show the transition from hydrated/amorphous structures to a connected Ba–O–Si framework during heat treatment. This is accompanied by the disappearance of OH/H_2O features and attenuation of carbonate bands, which is consistent with dehydration and $BaCO_3$ decomposition.

To assess the functional properties, we focused on powders synthesized at 100 °C (at atmospheric pressure) and subsequently heat-treated at 1000 °C. The resulting $BaSiO_3$ had particle sizes of 10–20 nm and 12–40 nm, and pore sizes of 2.3 and 1.96 nm, respectively. The powders exhibited high diffuse reflectance in the visible and near-infrared (NIR) spectrum and absorbance in the ultraviolet (UV) spectrum, which is consistent with a wide band gap (Eg ≈ 4.06–4.10 eV). Both amorphous and crystalline materials promoted the UV-driven degradation of methylene blue with comparable kinetics, indicating that nanoscale effects, such as short diffusion lengths and abundant surface sites, play a dominant role over long-range order. The wide band gap and high diffuse reflectance (~90%) varied only slightly upon heat treatment. The main microstructural change was coalescence-driven particle growth, accompanied by a decrease in specific surface area. Under UV irradiation, both phases exhibited high photocatalytic activity towards methylene blue, with comparable kinetics for amorphous and crystalline powders. Some reports describe pristine $BaSiO_3$ as a weak standalone photocatalyst, typically serving as a host in doped or composite systems [19,46]. However, under our experimental conditions, the nano-sized, MW-prepared $BaSiO_3$ acted as an independent UV photocatalyst for MB degradation. We attribute this to its nanoscale features and associated charge-transport/surface-reaction advantages.

Overall, MW-hydrothermal processing reduces the temperature and time required to obtain nano-sized $BaSiO_3$ and provides a clear structure–property relationship: rapid volumetric heating and pressure build-up enable early crystallization and narrow crystallite sizes; thermal treatment governs phase stabilization and densification.

The resulting nanoscale powders exhibit wide band gaps, high reflectance and efficient UV-driven dye degradation under the tested conditions. Therefore, photocatalytic activity is triggered by UV light rather than visible light. In practical terms, this restricts immediate use to UV-assisted settings (e.g., UV-LED or low-pressure Hg sources), whereas solar-driven operation would necessitate band-gap engineering (dopants/defects), photosensitization, or heterojunctions with visible-light semiconductors. It should be noted that reusability and long-term stability were not assessed here. Future work should evaluate multi-cycle MB degradation with intermediate washing, quantify retained activity and apparent rate constants, and perform post-test XRD, FT-IR, SEM and DRS to identify phase changes, carbonate accumulation, agglomeration or surface fouling, along with leaching assays (e.g., ICP-OES) to verify compositional stability.

Finally, to establish practical competitiveness, benchmarking against reference photocatalysts (e.g., TiO_2, ZnO) under identical conditions, including visible-light trials when band-gap modification is implemented, will be necessary.

5. Conclusions

A microwave–hydrothermal process was developed for synthesizing nano-sized powders of $BaSiO_3$ from aqueous precursors. Under these conditions, a crystalline $BaSiO_3$ phase was obtained at 240 °C, with domain sizes preserved in the range of tens of nanometres (10–27 nm). The materials exhibited high diffuse reflectance in the visible/near-IR range (approximately 90%) and a wide band gap (Eg = 4.11 eV for the sample dried at 150 °C,

Eg = 4.06 eV after calcination at 1000 °C, and an average Eg of approximately 4.09 eV). Under UV irradiation, both amorphous and crystalline powders catalyzed methylene blue (MB) decolourisation to 90–92% over fixed times (45 min for the amorphous powder and 60 min for the crystalline powder).

These outcomes are consistent with the processing–structure–property relationships identified in this study: rapid volumetric microwave heating and autogenous pressure promote early crystallization and smaller crystallite sizes at 240 °C. Subsequent thermal treatment then drives phase stabilization, coarsening and densification (BET decreases from 202 to 15.2 m^2 g^{-1} and pore volume from 0.016 to 0.0055 cm^3). In practice, the wide band gap implies UV-only activation under the present conditions. Future efforts will target visible-light operation (e.g., dopants/defects, photosensitisation, or heterojunctions), evaluate reusability and long-term stability through cycling and post-test characterization, and benchmark performance under identical conditions against reference photocatalysts (e.g., TiO_2, ZnO).

Author Contributions: Conceptualization, C.L., C.M.; technological development, experimental research, V.V.B.; theoretical researches, T.S.A.; experimental researches, A.A.P., physico-chemical researches, computer data handling, A.A.G., T.V.G.; scientific leader, A.A.S., writing—original draft preparation, A.A.S., T.S.A., C.L.; writing—review and editing, A.A.S., C.L. and C.M. All authors have read and agreed to the published version of the manuscript.

Funding: This research received no external funding.

Institutional Review Board Statement: Not applicable.

Informed Consent Statement: Not applicable.

Data Availability Statement: The data that support the findings of this study are available from the corresponding author upon reasonable request.

Acknowledgments: Authors would like to heartily acknowledge the support given by Mauro Zapparoli and Massimo Tonelli at CIGS, University of Modena and Reggio Emilia, Italy.

Conflicts of Interest: The authors declare no conflicts of interest.

References

1. Sridharan, S.; Tomozawa, M. Effect of various oxide additives on sintering of BaO-SiO_2 system glass-ceramics. *J. Mater. Sci.* **1992**, *27*, 6747–6754. [CrossRef]
2. Zhang, R.; Mao, H.; Taskinen, P. Thermodynamic descriptions of the BaO-CaO, BaO-SrO, BaO-SiO_2 and SrO-SiO_2 systems. *Calphad* **2016**, *54*, 107–116. [CrossRef]
3. Ramsden, A.H.; James, P.F. The effects of amorphous phase separation on crystal nucleation kinetics in BaO-SiO_2 glasses. *Mater. Sci.* **1984**, *19*, 1406–1419. [CrossRef]
4. Boulay, E.; Nakano, J.; Turner, S.; Idrissi, H.; Schryvers, D.; Godet, S. Critical assessments and thermodynamic modeling of BaO–SiO_2 and SiO_2–TiO_2 systems and their extensions into liquid immiscibility in the BaO–SiO_2–TiO_2 system. *Calphad-Comput. Coupling Phase Diagr. Thermochem.* **2014**, *47*, 68–82. [CrossRef]
5. Zhang, R.; Mao, H.; Halli, P.; Taskinen, P. Experimental phase stability investigation of compounds and thermodynamic assessment of the BaO–SiO_2 binary system and formation of barium silicates. *J. Mater. Sci.* **2016**, *51*, 4984–4995. [CrossRef]
6. Trusova, E.; Vaitkevičius, A.; Tratsiak, Y.; Korjik, M.; Mengucci, P.; Rinaldi, D.; Montalto, L.; Marciulionyte, V.; Tamulaitis, G. Barium and lithium silicate glass ceramics doped with rare earth ions for white LEDs. *Opt. Mater.* **2018**, *84*, 459. [CrossRef]
7. Asami, K.; Ueda, J.; Tanabe, S. Long persistent luminescence and blue photochromism in Eu^{2+}-Dy^{3+} co-doped barium silicate glass ceramic phosphor. *J. Lumin.* **2019**, *207*, 246–250. [CrossRef]
8. Gandhi, S.; Sakthivel, K.; Kwon, B.; Woo, H.; Lee, H.; Shin, D.; Jang, K. A novel efficient mesoporous silica assisted green emitting phosphors-an exotic remote phosphor with high quantum yield. *RSC Adv.* **2015**, *5*, 44192. [CrossRef]
9. Cao, D.; Wang, H.; Wei, H.; Yang, W. Preparation, electronic structure, and photoluminescent properties of Eu^{2+} activated $BaSi_2O_5$ powder phosphors for solid-state lighting. *J. Semicond.* **2015**, *36*, 123008. [CrossRef]

10. Nakamura, F.; Kantuptim, P.; Nakauchi, D.; Kato, T.; Kawaguchi, N.; Yanagida, T. Scintillation properties of $BaSiO_3$: Ce crystals by the floating zone method. *Mater. Res. Bull.* **2020**, *131*, 110961. [CrossRef]
11. Alsaif, N.; Al-Ghamdi, H.; Alfryyan, N.; Higazy, K.; Rammah, Y.; Kaky, K.; Kadhim, A.; Abouhaswa, A. Lutetium barium tellurite silicate glass samples doped with Fe_2O_3: Fabrication, physical, structure, and radiation attenuation capacity. *Opt. Mater.* **2024**, *159*, 116541. [CrossRef]
12. Guéguen, Y.; Houizot, P.; Célarié, F.; Chen, M.; Hirata, A.; Tan, Y.; Allix, M.; Chenu, S.; Roux-Langlois, C.; Rouxel, T. Structure and viscosity of phase-separated BaO–SiO_2 glasses. *J. Am. Ceram. Soc.* **2017**, *100*, 1982. [CrossRef]
13. Reis, S.T.; Schwartz, M.; Zandi, M.; Narendar, Y. Sanbornite-Based Glass-Ceramic Seal for High-Temperature Applications. U.S. Patent Application No. US20140295313A1, 2 October 2014.
14. Lisachuk, G.V.; Kryvobok, R.V.; Fedorenko, E.Y.; Zakharov, A.V. Ceramic radiotransparent materials on the basis of BaO-Al_2O_3-SiO_2 and SrO-Al_2O_3-SiO_2 systems. *J. Silic. Based Compos. Mater.* **2015**, *67*, 20–23. [CrossRef]
15. Xu, J.; Zhao, Y.; Chen, J.; Mao, Z.; Yang, Y.; Wang, D. Insights into the discrepant luminescence for $BaSiO_3$:Eu^{2+} phosphors prepared by solid-state reaction and precipitation reaction methods. *Luminescence* **2017**, *32*, 957–963. [CrossRef]
16. Romero-Serrano, A.; Cruz-Ramirez, A.; Zeifert, B.; Hallen-Lopez, M.; Hernandez-Ramirez, A. Thermodynamic modeling of the BaO–SiO_2 and SrO–SiO_2 binary melts. *Glass Phys. Chem.* **2010**, *36*, 171–178. [CrossRef]
17. Zhang, R.; Taskinen, P. Phase equilibria in the BaO-SiO_2-Al_2O_3 ternary system at 1500 °C. *Key Eng. Mater.* **2016**, *697*, 565–571. [CrossRef]
18. Yahia, I.S.; Zahran, H.Y.; Al-Ghamdi, A.A. Optical and structural properties of $BaSiO_3$ thin films prepared by solid state route. *Mater. Sci. Semicond. Process.* **2015**, *31*, 354. [CrossRef]
19. Taghrir, H.; Faghih, Z.; Ghashang, M.; Emami, L.; Dalili, S.; Khabnadideh, S. Barium silicate nanoparticles, an efficient catalyst for one-pot green synthesis of α-benzyl amino coumarin derivatives as potential chemotherapeutic agents. *RSC Adv* **2023**, *13*, 21127–21137. [CrossRef]
20. Galstyan, V.D.; Oganesyan, E.B.; Grigoryan, S.A.; Saxnazaryan, F.S.; Zolumyan, N.O. Izuchenie vzaimodeistviya v sisteme $BaC1_2$—Na_2SiO_3—H_2O pri 20 °C. *Armyanskiy Ximicheskiy J.* **1982**, *35*, 934–938.
21. Manvelyan, M.G.; Sarkisyan, A.S.; Sagatelyan, G.M. Sintez metasilikata bariya. *Izv. Arm.SSR Ximicheskie Nauk.* **1961**, *5*, 425.
22. Terzyan, A.M.; Melikyan, S.A.; Beglaryan, H.A.; Isahakyan, A.R.; Zulumyan, N.H. Barium silicates formation using silica hydrogel produced from serpentine minerals. *Chem. J. Armen.* **2018**, *71*, 517–523.
23. Zahedi, M.; Hassanzadeh-Tabrizi, S.A.; Saffar-Teluri, A. Sol-gel synthesis and luminescence properties of Ba_2SiO_4:Sm^{3+} nanostructured phosphors. *Ceram. Int.* **2018**, *44*, 10169–10174. [CrossRef]
24. Beglaryan, H.A.; Melikyan, S.A.; Zulumyan, N.H.; Terzyan, A.M.; Isahakyan, A.R. Influence of colloid synthesis techniques on barium silicates formation using silica hydrogel derived from serpentine minerals. *J. Mol. Liq.* **2019**, *291*, 111263. [CrossRef]
25. Merzhanov, A.G.; Rogachev, A.S.; Sychev, A.E. Self-Propagating High-Temperature Synthesis: First Space Experiments. *Dokl. Phys. Chem.* **1998**, *362*, 299–303.
26. Sherikar, B.N.; Sahoo, B.; Umarji, A.M. One-step synthesis of diopside ($CaMgSi_2O_6$) ceramic powder by solution combustion method. *Adv. Powder Technol.* **2020**, *31*, 2875. [CrossRef]
27. Salehtash, F.; Jalaly, M.; Emrooz, H.B.M.; Gotor, F.J.; Sayagués, M.J. Mesoporous silica by solution-combustion synthesis followed by etching. *Int. J. Self-Propagating High-Temp. Synth.* **2018**, *27*, 221–227. [CrossRef]
28. Coccia, F.; Mascitti, A.; Rastelli, G.; d'Alessandro, N.; Tonucci, L. Sustainable photocatalytic reduction of maleic acid: Enhancing CuxO/ZnO stability with polydopamine. *Appl. Sci.* **2025**, *15*, 1631. [CrossRef]
29. Tsuzuki, T. Mechanochemical. Synthesis of metal oxide nanoparticles. *Commun. Chem.* **2021**, *4*, 143. [CrossRef]
30. Leonelli, C.; Colombini, E.; Mortalò, C. Contribution of microwave irradiation in the synthesis of inorganic compounds: An Italian Approach. *Inorganics* **2025**, *13*, 410. [CrossRef]
31. Riva, V.; Boccaccini, D.; Cannio, M.; Maioli, M.; Valle, M.; Romagnoli, M.; Mortalò, C.; Leonelli, C. Insight into t→m transition of MW treated 3Y-PSZ ceramics by grazing incidence X-Ray diffraction. *J. Eur. Ceram. Soc.* **2022**, *42*, 227–237. [CrossRef]
32. Mortalò, C.; Rosa, R.; Veronesi, P.; Fasolin, S.; Zin, V.; Deambrosis, S.M.; Miorin, E.; Dimitrakis, G.; Fabrizio, M.; Leonelli, C. Microwave assisted sintering of Na-β″-Al_2O_3 in single mode cavities: Insights in the use of 2450 MHz frequency and preliminary experiments at 5800 MHz. *Ceram. Int.* **2020**, *46*, 28767–28777. [CrossRef]
33. Kappe, C.O. My twenty years in microwave chemistry: From kitchen ovens to microwaves that aren't Microwaves. *Chem. Rec.* **2019**, *19*, 15–39. [CrossRef] [PubMed]
34. Varma, R.S. "Greener" chemical syntheses using mechanochemical mixing or microwave and ultrasound irradiation. *Green Chem. Lett. Rev.* **2007**, *1*, 37–45. [CrossRef]
35. Bilecka, I.; Niederberger, M. Microwave chemistry for inorganic nanomaterials synthesis. *Nanoscale* **2010**, *2*, 1358. [CrossRef]
36. Petrova, E.M.; Yusunova, L.M.; Bogacheva, T.M.; Axmedyanova, R.A.; Liakumovich, A.G. Effekt mikrovolnovogo izlucheniya v ximicheskix reakciyax. *Sovrem. Nauk. Texnologii* **2015**, *18*, 28–32.

37. Jawor, A.; Jeong, B.H.; Hoek, E.M.V. Synthesis, characterization, and ion-exchange properties of colloidal zeolite nanocrystals. *J. Nanopart. Res.* **2009**, *11*, 1795. [CrossRef]
38. Hu, M.Z.; Khatri, L.; Harris, M.T. Monodispersed ultrafine zeolite crystal particles by microwave hydrothermal synthesis. *Ceram. Trans.* **2009**, *208*, 91. [CrossRef]
39. Tränkle, S.; Jahn, D.; Neumann, T.; Hüsing, N.; Volkmer, D. Conventional and microwave assisted hydrothermal syntheses of 11 Å tobermorite. *J. Mater. Chem. A* **2013**, *1*, 10318. [CrossRef]
40. Thostenson, E.T.; Chou, T.W. Microwave processing: Fundamentals and application. *Compos. Part A: Appl. Sci. Manuf.* **1999**, *30*, 1055–1071. [CrossRef]
41. Brittany, H. *Microwave Synthesis*; CEM Publishing: Matthews, NC, USA, 2002; Volume 296.
42. Bagramyan, V.V.; Sargsyan, A.A.; Ponzoni, C.; Rosa, R.; Leonelli, C. Microwave-assisted preparation of sodium-silicate solutions from perlite. *Theor. Found. Chem. Eng.* **2015**, *49*, 731–735. [CrossRef]
43. Aghamalyan, N.R.; Sargsyan, A.A.; Azatyan, T.S.; Grigoryan, T.V.; Kazaryan, A.A.; Petrosyan, A.A.; Gyulasaryan, H.T.; Kafadaryan, Y.A.; Nersisyan, M.N.; Knyazyan, N.B.; et al. Photocatalytic and radiation-optical properties of lead metasilicate obtained by the microwave method. *J. Contemp. Phys.* **2024**, *59*, 199–207. [CrossRef]
44. Grishina, A.N.; Kozlova, E.V.; Satyukov, A.B. Issledovanie sostava nanorazmernix gidrosilikatov bariya s primeneniem IK-spektroskopii. *Mejdunarodniy Nauchno-Issledovatelskiy J.* **2013**, *8*, 19.
45. Shen, K.; Zhang, R.; Jin, Y.; Li, Y.; Hu, Y. Inorganic metal oxide material $BaSiO_3$:Eu^{2+} for convenient 3D X-ray imaging. *J. Lumin.* **2024**, *269*, 120536. [CrossRef]
46. Hu, X.; Lu, P.; Fu, M.; Zhang, Y.; Cao, X.; Chen, J.; Lin, S.; Yao, J.; Zhang, Z. Activating the photocatalytic activity of insulator barium silicate: A liquid-phase alkalized tetracycline photosensitizer and its self-destruction. *Chem. Eng. J.* **2023**, *454*, 140281. [CrossRef]
47. Paradisi, E.; Mortalò, C.; Zin, V.; Armetta, F.; Boiko, V.; Hreniak, D.; Zapparoli, M.; Deambrosis, S.M.; Miorin, E.; Leonelli, C.; et al. Eu-Doped YPO_4 luminescent nanopowders for anticounterfeiting applications: Tuning morphology and optical properties by a rapid Microwave-Assisted Hydrothermal Method. *ACS Appl. Nano Mater.* **2024**, *7*, 6893–6905. [CrossRef]
48. Paradisi, E.; Mortalò, C.; Zin, V.; Deambrosis, S.M.; Zapparoli, M.; Miorin, E.; Leonelli, C. Understanding the effect of temperature on the crystallization of Eu^{3+}:YPO_4 nanophosphors prepared by MW-Assisted Method. *Ceram. Int.* **2025**, *51*, 7075–7086. [CrossRef]